

**Title: Fast Patch-Based Pseudo-CT Synthesis from T1-Weighted
MR Images for PET/MR Attenuation Correction in Brain Studies**

Running Title: MRI-Based Pseudo-CT Synthesis for PET/MR

Angel Torrado-Carvajal^{1,2}, Joaquin L. Herraiz^{2,3}, Eduardo Alcaín⁴, Antonio S.
Montemayor⁴, Lina Garcia-Cañamaque⁵, Juan A. Hernandez-Tamames^{1,2}, Yves
Rozenholc⁶, Norberto Malpica^{1,2}

¹ Medical Image Analysis and Biometry Lab, Universidad Rey Juan Carlos, Madrid, Spain

² Madrid-MIT M+Vision Consortium, Madrid, Madrid, Spain

³ Research Laboratory of Electronics, Massachusetts Institute of Technology, Cambridge, MA, USA

⁴ Dept. of Computer Science, Universidad Rey Juan Carlos, Mostoles, Madrid, Spain

⁵ Hospital Universitario HM Puerta del Sur, HM Hospitales, Mostoles, Madrid, Spain

⁶ MAP5, CNRS UMR 8145, University Paris Descartes, Paris, Paris, France

Corresponding Author: Angel Torrado-Carvajal

**Postal Address: Medical Image Analysis and Biometry Lab
Universidad Rey Juan Carlos
C/ Tulipan s/n
2833, Mostoles
Spain**

E-mail Address: angel.torrado@urjc.es

Telephone: +34 91 488 85 10

Fax: +34 91 488 70 49

Word Count: 5,492

Abstract:

Attenuation correction in hybrid PET/MR scanners is still a challenging task. This paper describes a methodology for synthesizing a pseudo-CT volume from a single T1 weighted volume, thus allowing us to create correct AC maps.

Methods.

We propose a fast pseudo-CT generation from a patient-specific MRI T1-weighted image using a group-wise patch-based approach and a MRI-CT atlas dictionary. For every voxel in the input MR image, we compute the similarity of the patch containing that voxel with the patches of all MR images in the database, that lie in a certain anatomical neighborhood. The pseudo-CT is obtained as a local weighted linear combination of the CT values of the corresponding patches. The algorithm was implemented in a Graphical Processing Unit (GPU).

Results.

We evaluated our method both qualitatively and quantitatively for PET/MR correction. The approach performed successfully in all cases considered. We compared the SUVs of the PET image obtained after attenuation correction using the patient specific CT volume, and using the corresponding computed pseudo-CT volume. The voxel by voxel correlation between SUV obtained with both methods was very high ($R^2=0.9980$, $p<0.0001$), while the Bland-Altman test showed that the average of the differences was very low (0.0006 ± 0.0594). A region of interest analysis was also performed. The

correlation between mean SUV value and maximum SUV value of every region was very high ($R^2=0.9989$, $p<0.0001$ and $R^2=0.9904$, $p<0.0001$, respectively).

Conclusions.

Results indicate how our method can accurately approximate the patient-specific CT and may serve as a potential solution for accurate attenuation correction in hybrid PET/MR systems. The quality of the corrected PET using our pseudo-CT is comparable to having acquired a patient-specific CT, thus, improving the results obtained with the UTE-based attenuation correction maps currently used in the mMR scanner. The GPU implementation led to a substantial decrease in computational time making the approach suitable for real applications.

Keywords: Pseudo-CT, image synthesis, PET/MR, attenuation correction, GPU.

INTRODUCTION

Positron Emission Tomography (PET) performs functional imaging by detecting pairs of annihilation gamma rays emitted indirectly by a positron-emitting radionuclide (radiotracer), allowing the measurement of the radiotracer biodistribution. Magnetic Resonance Imaging (MRI) provides, among others, detailed morphological imaging of organs or soft tissue, with excellent spatial resolution. The evolution of both modalities into complementary in vivo molecular imaging techniques has produced increased interest in the development of hybrid MR/PET systems (1).

The construction of accurate attenuation correction maps (AC maps) is essential for the clinical application of hybrid PET/MR systems. Constructing PET AC maps for use in those hybrid systems is challenging because no direct relation exists between PET attenuation coefficients (μ) and MR signal intensity (2), contrary to what happens with AC maps and the intensity of CT images (3). Additionally, treating bone as soft tissue in MR-derived AC maps for PET/MR attenuation correction leads to a substantial underestimation in the analysis of PET tracer distribution (4). Creating a pseudo-CT (pCT) from MRI data could help to produce an accurate AC map, with a quality comparable to having acquired a real CT of the patient.

Previous approaches for MRI-based AC have been presented in the literature (5). They mainly differ on the type of semantic representation that is used to describe the image data, based on mathematical morphology (6), deformable models (7), MRI Dixon (8) or Ultrashort TE (UTE) sequences (9,10), and multi-atlas segmentation using label-fusion (11). However, most of these methods showed limited accuracy when used to create AC maps (12). Hofmann et al. combined local pattern recognition with

image registration to generate pCT images (13). Recently, Izquierdo-Garcia et al. proposed an approach to pCT synthesis based on non-rigid registration to an atlas using the standard SPM8 software with a CT template (14). Burgos et al. described an improved method that used non-rigid registration to an atlas, followed by label-fusion based on patch-similarity measurements (15). Furthermore, clinical scanners currently rely on multiple MR sequence acquisition, but the results are not fully reliable, as shown in (16).

Recently, patch-based methods have shown to be a versatile segmentation technique (17). Patch-based segmentation was introduced as an alternative approach for label propagation which eliminates the requirement of non-rigid registration. This technique was developed as an adaptation of the non-local framework developments for non-local denoising (18). Several approaches have been introduced depending on the patch fusion methods or rules (19,20). Ye et al. proposed a patch-based method for generating a T2 volume from a T1-weighted volume (21).

In this work, we propose a simple and fast approach for pCT synthesis from a single patient-specific MRI T1-weighted image using a group-wise patch-based approach and a limited MRI and CT atlas dictionary. Our method is purely patch-based, eliminating the need of a registration step. This allows a considerable reduction of time. Also, the algorithm becomes parallelizable, so that a fast implementation using a Graphical Processing Unit (GPU) card is presented.

In the next section we describe the data set used in this work and the overall process of the pCT synthesis and AC maps. Then, we present different experiments quantitatively comparing the use of patient-specific CT and our pCT for AC correction.

Finally we discuss the findings from the experimental results and the possible implications for managing PET AC in hybrid PET-MR systems, and extract some conclusions.

MATERIALS AND METHODS

Patient Population

The institutional review board-approved retrospective study included a data set containing 19 healthy volunteers (19 females, mean age (34.96 ± 5.23) y, range: 27 y – 46 y). All of them underwent both MRI and CT imaging. For this type of study, the need for written informed consent was waived.

Image Acquisition

MRI images of the head were acquired on a General Electric Signa HDxt 3.0T MR scanner using the body coil for excitation and an 8-channel quadrature brain coil for reception. Imaging was performed using an isotropic 3DT1w SPGR sequence with a TR=10.024ms, TE=4.56ms, TI=600ms, NEX=1, acquisition matrix=288x288, resolution=1x1x1mm, and flip angle=12°.

Low-dose CT images were acquired on a Siemens Somatom Sensation 16 CT scanner with matrix=512x512, resolution=0.48x0.48mm, slice thickness=0.75mm, PITCH=0.7mm, acquisition angle=0°, voltage=120kV, radiation intensity=200mA.

Data Pre-Processing

Image pre-processing was carried out using 3D Slicer built-in modules (22). This pre-processing included: MRI bias correction (N4 ITK MRI bias correction), rigid

registration (general registration BRAINS) to align each patient-specific MRI-CT pair, rigid registration to pre-align all the images in the same spatial origin – all the images are set in the same orientation –, and normalization of the greyscale values (ITK-based histogram matching).

Pseudo-CT Synthesis

Weights Estimation. Let I be an input image to be processed, and A an anatomy atlas containing a set of MRI T1-weighted volumes I_{MR} and their corresponding I_{CT} volumes: $A = \{(I_{MR}^i, I_{CT}^i) \mid i = 1, \dots, n\}$.

Let us consider w_i as a weight reflecting non-local similarities between voxels $\mathbf{a} = (a_x, a_y, a_z)$ in the input image I and voxels $\mathbf{b} = (b_x, b_y, b_z)$ in the image I_{MR}^i of the atlas A over the image domain Ω , and computed using the following equation:

$$w_i(\mathbf{a}, \mathbf{b}) = f \left(\frac{\sum_{\mathbf{a}' \in P_I(\mathbf{a}), \mathbf{b}' \in P_{I_{MR}^i}(\mathbf{b})} (I(\mathbf{a}') - I_{MR}^i(\mathbf{b}'))^2}{2S\beta\hat{\sigma}^2} \right) \quad (1)$$

where $P_I(\mathbf{a})$ is a 3D patch of the image I centered at voxel \mathbf{a} , S is the number of voxels in the 3D patch, β is a smoothing parameter, and $\hat{\sigma}$ is the standard deviation of the noise. The original denoising approach assumes that similarities of a patch can be found over the entire image domain Ω . However, in our context of modality propagation, the variations of the anatomical structures in a population are bounded, so we can find good matches in a specific neighbourhood $N_{m \times m \times m}(\mathbf{a})$ of a certain voxel \mathbf{a} . The weights are then estimated in this local area as $w = \{w(\mathbf{a}, \mathbf{b}), \forall \mathbf{a} \in \Omega, \mathbf{b} \in N_{m \times m \times m}(\mathbf{a})\}$, reflecting the local similarities between I and $\{I_{MR}^i\}_{i=1, \dots, n}$.

The size of the patch has been set to 3x3x3 for all experiments. The size of the considered neighborhood has been set to 11x11x11, which is directly related to the head anatomical variability (21).

Group-Wise Label Propagation. Once the weights have been computed using equation 1. By using those weights, the corresponding voxel \mathbf{a} of image $I_{pseudoCT}$ can be estimated as a weighted linear group-wise combination of the patches in I_{CT}^i as follows:

$$\forall \mathbf{a} \in \Omega, I_{pseudoCT}(\mathbf{a}) = \frac{\sum_{i=1}^n \sum_{\mathbf{b} \in N_{m \times m \times m}(\mathbf{a})} w(\mathbf{a}, \mathbf{b}) I_{CT}^i(\mathbf{b})}{\sum_{i=1}^n \sum_{\mathbf{b} \in N_{m \times m \times m}(\mathbf{a})} w(\mathbf{a}, \mathbf{b})} \quad (2)$$

Which takes all the images I_{MR}^i in the atlas A to produce a group-wise combination of I_{CT}^i , thus, obtaining an estimation of $I_{pseudoCT}$.

Regularization. Contrary to registration-based approaches, if there is no correspondence between the patch of the input image I and the patches of the images I_{MR}^i in the atlas A , no value (NaN due to division by 0) is assigned to the voxel \mathbf{a} of $I_{pseudoCT}$.

This situation makes it necessary to include a regularization step that deals with non-labeled voxels. Usually these cases are isolated, so in this work we have assigned to this voxel the value of the median in its neighbourhood. The size of this new neighbourhood has been set to 3 in this paper, so that $N_{3 \times 3 \times 3}(\mathbf{a})$.

$$\forall \mathbf{a} = \mathbf{NaN} \in \Omega, I_{pseudoCT}(\mathbf{a}) = \mathit{median}_{N_{3 \times 3 \times 3}(\mathbf{a})} (I_{pseudoCT}(\mathbf{a})) \quad (3)$$

GPU Implementation

The Patch-Based algorithm is highly parallelizable. The calculation of the resulting $I_{pseudoCT}$ for each voxel I in the 3D input volume is completely independent from the other voxels. Configuring a 3D grid in a CUDA model allows eliminating loops to iterate over the different voxels in the volume. Our CUDA kernel contains the selection of atlas A , and the search in the neighborhood N ; this way, each label calculation is performed in a separate thread.

PET Simulation

We obtained detailed tissue segmented models from the T1-weighted volumes by using the pipeline described by Torrado-Carvajal et al. (23). These models contained cerebellum WM and GM, brain WM and GM, CSF, skull, eyes, muscle, fat, and skin. We assigned a standard FDG-PET activity to each tissue according to these relative values (GM: 4.0, WM and rest of soft tissue: 1.0, CSF and bone: 0.0) (24,25) obtaining the ground truth PET maps. Then, these ground truth maps were projected with the 3D-OSEM software (26) assuming the geometry, parameters and sinogram format of the Biograph mMR scanner (27). The system response matrix used in this case assumed a uniform gaussian point-spread function (PSF) with 4 mm FWHM in the whole FOV. As in Hofmann et al., we neglected scatter and random coincidences to isolate the effect of the attenuation maps in the final reconstructed PET images (13). The projection data generated were our attenuation-free reference data.

The 511-keV AC maps derived from the CT (gold standard) and from the MR (pCT) images and originated using the conversion described in Nakamoto et al. (28) were forward projected generating the attenuation data. The forward projection is based on the same code used for projecting the PET distribution with the 4-mm PSF, as the blurring effects involved in the PET emission, like positron range and non-co-linearity, affect also the attenuation of the gamma-rays. We then used these two projection data sets ($Proj_{\mu MR}$ and $Proj_{\mu CT}$) to generate our attenuation-corrected data (PET_{MR-AC}) from the attenuation-free one (PET) following equation:

$$PET_{MR-AC} = PET e^{(Proj_{\mu MR} - Proj_{\mu CT})} \quad (4)$$

Image Reconstruction

The attenuated projection data and the attenuation-free data were both reconstructed with the 3D-OSEM software (26) adapted to the geometry and sinogram size of the mMR scanner. We used 30 iterations and 3 subsets and the reconstructed images consisted of 201x201x129 voxels of 2x2x2 mm each. As indicated in Burger et al., the differences between these two reconstructed images depends on the reconstruction method used, but it is outside of the scope of this work to analyse this effect (3).

Experimental Setup

The available data were separated into an atlas A containing 10 MRI-CT pairs $A = \{(I_{MR}^i, I_{CT}^i) \mid i = 1, \dots, 10\}$, and a test set T containing the 9 remaining MRI-CT pairs $T = \{(I_{MR}^j, I_{CT}^j) \mid j = 1, \dots, 9\}$.

RESULTS

Image Quality

Figure 1 shows a complete head MRI volume, the ground truth and the synthesized pCT for two healthy subjects. Visual inspection evaluation was performed by an expert radiologist to confirm the accuracy of our method; our pipeline works equally well in all cases considered.

The proposed method estimates the shape of the skull generally well, despite patient-specific anatomical variations. The comparison between the patient-specific CT and the pCT shows that our method is able to accurately estimate the ground truth, delimiting the skull contours and differentiating air from bone. Visual inspection of the results shows the high quality of the pCT estimation and the robustness of the method, which is able to capture the details of the bone spikes in non-smooth areas such as the sinuses or the cervical vertebrae.

We also tested the effect of changing the size of the atlas on the quality of the synthesized images in subjects without skull deformations, using atlas of 5, 7, and 10 datasets (Figure 2). We used the normalized cross correlation (NCC) to quantitatively measure the quality of the synthesized pseudo-CTs (I_2) compared to the ground truth CT (I_1) following equation 5.

$$NCC = \frac{1}{N} \sum_{x,y} \frac{(I_1(x,y) - \mu_1)(I_2(x,y) - \mu_2)}{\sigma_1 \sigma_2} \quad (5)$$

The experimental NCC was 0.9281 ± 0.0066 for the atlas with 5 datasets, 0.9294 ± 0.0051 for the atlas with 7 datasets, and 0.9324 ± 0.0048 for the atlas with 10 datasets.

Artifacts caused by dental restorations are a common problem in MRI and CT scans of the head and neck. Those implants impair CT image quality due to beam hardening artifacts; likewise, they impair MRI image quality resulting in signal loss. The presence of an implant in the jaw of a subject results in signal loss in the MRI, beam hardening in the CT and blurring in the synthesized pCT (Figure 3).

PET Correction Quality

Voxel by Voxel Analysis. Voxel by voxel analysis was performed to determine differences in reconstructed Standardize Uptake Values (SUVs) for all test subjects. Comparison of the attenuation-free SUV images (Gold Standard) –attenuated and corrected with the patient-specific CT– and the pCT-based corrected SUV images –attenuated with the patient-specific CT and corrected with the synthesized pCT– showed excellent correlation. Errors are lower than 10% of the SUVs in most voxels. Some deviations can be appreciated in subjects A and B, but the error is lower than 5% on average (Figure 4).

We also computed the voxel by voxel correlation between pCT-based SUV versus CT-based SUV and the Bland-Altman of SUV measurements for all 9 test subjects over the whole head (Figure 5). Voxels dominated by noise ($SUV < 0.01$) were not included in the analysis. The correlation plot shows an excellent correlation between SUV

obtained with both methods ($R^2=0.9980$, $p<0.0001$). The Bland-Altman plot shows that the average of the differences is very low (0.0006 ± 0.0594); the difference between methods tend to get smaller as the average increases, accumulating the error in voxels with low SUV values.

Region of Interest (ROI) Analysis. ROI analysis was performed to determine differences in assigned attenuation coefficients and reconstructed SUVs. ROIs were defined as the original segmented tissues used to assign PET activity in the simulation.

Table 1 provides a summary of pCT-based and CT-based attenuation coefficient values for each ROI analysed. Paired-samples Wilcoxon signed rank tests were performed to assess if pCT-based and CT-based attenuation coefficient values mean ranks differed. No significant differences were found in the mean CT-based attenuation coefficients, as compared to assigned pCT-based attenuation coefficients, in all ROIs except for the skin.

We computed the correlation between pCT-based SUV versus CT-based SUV and the Bland-Altman of the mean and maximum SUV measurements for each region of interest (Figure 6). The correlation plot for mean SUV shows an excellent correlation between mean SUV obtained with both methods ($R^2=0.9989$, $p<0.0001$). The Bland-Altman plot for mean SUV shows that the average of the differences is very low (0.0009 ± 0.0338); the difference between methods does not show an increasing or decreasing trend as the average changes. The correlation plot for max SUV shows a very slight overestimation in the max SUV obtained with our method ($R^2=0.9904$, $p<0.0001$). The Bland-Altman plot for max SUV shows that the average of the

differences is low (0.0312 ± 0.2345); the difference between methods confirms a slight overestimation of our method in regions with low SUV values.

Experiments on Clinical Data

To perform a validation on real data, we acquired MR, PET and CT volumes of a subject. The institutional review board (Fundación HM Hospitales) approved this study and the subject signed a written informed consent.

MR and PET images of the head were acquired on a Siemens Biograph mMR scanner using the body coil for excitation and an 8-channel quadrature brain coil for reception. We acquired a 3DT1w MP-RAGE volume with TR=1800ms, TE=2.65ms, TI=900 ms, NEX=1, acquisition matrix=250x250x250, resolution=1x1x1mm, flip angle=9°. Furthermore, a double UTE sequence with TR=11.94ms, TE1=0.07ms, TE2=2.46ms, NEX=1, acquisition matrix=192x192x192, resolution=1.56x1.56x1.56mm, flip angle=10°, as well as a Dixon sequence with TR=3.6ms, TE1=1.23ms, TE2=2.46ms, acquisition matrix=192x126x128, resolution=2.08x2.08x2.34mm, flip angle=10° were acquired to obtain the AC map.

Low-dose CT images were acquired on a Toshiba Aquilion PRIME CT scanner with matrix=512x512, resolution=0.43x0.43mm, slice thickness=1mm, PITCH=0.62mm, acquisition angle=0°, voltage=120kV, radiation intensity=200mA.

The subject was administered 129.1 MBq of fluorodeoxyglucose (18F-FDG). PET data were acquired 20 minutes after the injection over a single bed position for 15 minutes. The images without attenuation correction were reconstructed using the iterative

algorithm OP-OSEM provided by the manufacturer with 6 iterations and 21 subsets, reconstruction matrix= $344 \times 344 \times 127$, resolution= $2.09 \times 2.09 \times 2.03$ mm. The reconstruction includes a point spread function (PSF) model.

We synthesized the pCT volume using the atlas with 10 volume pairs and the same processing pipeline as in previous experiments. The reconstructed image without attenuation correction was projected with the same code used in the previous section. The resulting sinograms were then corrected by attenuation using the three different maps (CT-based, UTE- μ MAP and pCT-based). The corrected sinograms were reconstructed with the 3D-OSEM algorithm with 30 iterations and 1 subset, reconstruction matrix= $127 \times 127 \times 127$, resolution= $2 \times 2 \times 2$ mm.

Figure 7 shows the MR, the CT, the UTE- μ MAP and the pCT images and the result of correcting the PET data with the different volumes. The NCC was 0.5808 between the CT and the UTE- μ MAP, and 0.8919 between the CT and the pCT.

Computational Time

For a $271 \times 271 \times 221$ volume, the complete time to synthesise the pCT volume for different number of images in the multi-atlas case is shown in Table 2. In the worst-case scenario (atlas of 10 volumes), computation of the pCT volume in GPU takes less than 9 minutes, x4374 less time than with a Matlab implementation, x27 less than using a C implementation and x11 less than with an OpenMP multithreaded C version using 32 threads.

All the experiments were performed on a 3.1GHz Intel Xeon-E5 2687W, with 128 GB RAM and Windows Server 2008 R2 powered with an NVIDIA Tesla k20x GPU.

DISCUSSION

The generation of accurate AC maps is a basic step for PET/MRI quantification. However, ignoring bone is known to cause a distorted and biased distribution of the reconstructed SUV. Several approaches have been proposed, based mainly in a combination of MR sequences or using image registration to take advantage of a priori acquired CT data. Methods requiring the acquisition of additional MR data show a significant underestimation of activity concentration. Approaches based on non-rigid image registration are computationally intensive and are normally unable to deal with local changes in anatomy, due to pathology or implants.

We propose the use of a patch-based method for synthesizing a pCT volume from a single T1 MR volume. Compared to non-rigid registration methods, the patch-based approach uses only information from those volumes in the atlas that actually match the patch, preventing errors due to misregistration, making it able to deal with local morphological changes in the images.

Our results are in line with those recently described in Burgos et al. (15). However, our method eliminates the need of image registration, providing results with the same accuracy, while allowing to implement a much faster algorithm.

We have evaluated our method both qualitatively and quantitatively for PET/MR correction. The visual (Figure 1) and quantitative (Figure 4) image quality analysis performed show that CT and pCT are very similar. The high NCC values indicate how our method can accurately approximate the patient-specific CT. We have also shown an example on a subject with a dental restoration, providing better results than CT-based AC maps (Figure 3). No significant differences were found in all ROIs except the skin, where the deviation was -0.006126 ± 0.004088 , $p\text{-value}=0.0039$ (Table 1); this can be due to the fact that the skin is the thinnest ROI, so small errors in the estimation of the region can have a large effect on the result. As the CT is not going to be used for diagnostic purposes, the level of detail of the pCT does not need to be equivalent to a real acquired CT.

It can be noticed that the attenuation coefficients that we derived in both cases from the Hounsfield values using the transformation proposed by Nakamoto et al. (28) differ slightly from the values assigned to these tissues in other publications. However, our results are independent of the transformation used, as we are comparing the pCT generated by our method to a gold standard CT, and the same transformation is used in both volumes to obtain the attenuation values.

Analysis of the absolute error maps (Error = pCT-based – CT-based) confirmed there are small differences between both approaches, which are mainly localized in the air interface zones where the PET activity is low and usually non-relevant for clinical applications (Figure 4). The ROI analysis shows a strong correlation between attenuation-free SUV images and pCT-based corrected SUV images (Figure 6). In this work, we only considered a standard ^{18}F -FDG biodistribution to evaluate the final

impact of the method in a normal PET brain scan, but we expect similar small deviations with other radiotracers.

We have also tested our method on real clinical data. Using the real CT volume of the subject as a gold standard, we have compared the pCT image obtained with our method and the UTE- μ MAP currently used for attenuation correction in the mMR scanner. The UTE- μ MAP is not able to differentiate air from bone in certain regions, leading to errors in the final PET image (Figure 7). The NCC for the clinical data is lower than that from the test data, possibly due to the different scanners and sequences used to acquire the clinical data and the atlas volumes. As future research, we will design similarity measures that are robust to such changes.

There are some other effects that we have neglected. One is the impact of the possible deviations in the MR-derived attenuation map when the scatter correction is considered. The distribution of scatter in the sinogram is usually very smooth. The effects of deviations in the μ -map on the scatter correction are averaged over many sinogram bins. Therefore, small deviations in the attenuation map will have a very modest impact on the scatter correction, especially as the scaling factor used to fit the estimated scatter distribution to the experimental data would remove any overall bias that may be introduced. We also did not include the effect of possible errors in the modelling of the attenuation of the MR-Coils (12). However, this effect can be controlled in clinical practice with the appropriate scanner modelling, calibrations and acquisition protocols.

The method is highly parallelizable, as each voxel is computed independently. This has allowed implementing a GPU version that provides a complete pCT in times similar

to those that would be needed for acquiring an actual CT scan. There is still room for improvement in the GPU implementation, so some speedup of the algorithm is still possible.

We have validated our approach using a set of 10 whole head volume pairs in healthy subjects, in contrast to typical brain studies that do not include the neck, which is very difficult to synthesize due to its anatomical complexity and variability.

Our technique could, in theory, be applied in other regions of the body. Registration-based approaches are not so straightforward as our approach in other regions, due to stronger inter-subject anatomical differences. In a real clinical application, the atlas should be designed to include the necessary anatomical heterogeneity. The design of specific databases that take into account skull lesions will be a future line of research. However, our study suggests that SUVs measured on PET/MR and those measured on PET/CT are close enough; this finding makes our approach feasible for qualitatively interpretation of PET scans for diagnostic purposes. The method should be further validated on images with distinct regions, such as tumours.

CONCLUSION

In this work we showed how the use of patch-based techniques to estimate a pseudo-CT from MR T1-weighted images allows determining accurate AC maps for use in hybrid PET/MR systems. The proposed method provides an accurate estimation of a pseudo-CT with similar accuracy to the patient-specific CT, without the need of a registration step. Atlas-based approaches avoid the over-simplification of most previous proposed methods based on segmented MR images that assume that all voxels in the same tissue type should have the same attenuation coefficients. The GPU implementation led to a substantial decrease in computational time making the approach suitable for real applications.

ACKNOWLEDGEMENT

The authors thank the anonymous reviewers for their valuable comments and suggestions that helped to improve the quality of the study. This project has been partially supported by Consejería de Educación, Juventud y Deporte de la Comunidad de Madrid through the Madrid-MIT M+Visión Consortium and the Seventh Framework Programme of the European Union, and project TEC2012-39095-C03-01 of the Spanish Ministry of Economy and Competitiveness.

REFERENCES

1. Shao Y, Cherry SR, Farahani K, et al. Simultaneous PET and MR imaging. *Phys Med Biol.* 1997;42:1965-1970.
2. Wagenknecht G, Kaiser HJ, Mottaghy FM, Herzog H. MRI for attenuation correction in PET: methods and challenges. *Magn Reson Mater Phys.* 2013;26:99-113.
3. Burger C, Goerres G, Schoenes S, Buck A, Lonn AH, Von Schulthess GK. PET attenuation coefficients from CT images: experimental evaluation of the transformation of CT into PET 511-keV attenuation coefficients. *Eur J Nucl Med Mol Imaging.* 2002;29:922-7.
4. Andersen FL, Ladefoged CN, Beyer T, et al. Combined PET/MR imaging in neurology: MR-based attenuation correction implies a strong spatial bias when ignoring bone. *Neuroimage.* 2014;84:206-216.
5. Hofmann M, Pichler B, Schölkopf B, Beyer T. Towards quantitative PET/MRI: a review of MR-based attenuation correction techniques. *Eur J Nucl Med Mol Imaging.* 2009;36:93-104.
6. Dogdas B, Shattuck DW, Leahy RM. Segmentation of skull and scalp in 3-D human MRI using mathematical morphology. *Hum Brain Mapp.* 2005;26:273-285.
7. Wang D, Shi L, Chu WC, Cheng JC, Heng PA. Segmentation of human skull in MRI using statistical shape information from CT data. *J Magn Reson Imaging.* 2009;30:490-498.

8. Martinez-Möller A, Souvatzoglou M, Delso G, et al. Tissue classification as a potential approach for attenuation correction in whole-body PET/MRI: evaluation with PET/CT data. *J Nucl Med.* 2009;50:520-526.
9. Robson MD, Bydder GM. Clinical ultrashort echo time imaging of bone and other connective tissues. *NMR Biomed.* 2006;19:765-780.
10. Keereman V, Fierens Y, Broux T, De Deene, Y, onneux M, Vandenberghe S. MRI-based attenuation correction for PET/MRI using ultrashort echo time sequences. *J Nucl Med.* 2010;51:812-818.
11. Torrado-Carvajal A, Herraiz JL, Hernandez-Tamames JA, et al. Multi-atlas and label fusion approach for patient-specific MRI based skull estimation. *Magn Reson Med.* DOI: 10.1002/mrm.25737.
12. Visvikis D, Monnier F, Bert J, Hatt M, Fayad H. PET/MR attenuation correction: where have we come from and where are we going?. *Eur J Nucl Med Mol Imaging.* 2014;41:1172-5.
13. Hofmann M, Steinke F, Scheel V, et al. MRI-based attenuation correction for PET/MRI: a novel approach combining pattern recognition and atlas registration. *J Nucl Med.* 2008;49:1875-1883.
14. Izquierdo-Garcia D, Hansen AE, Förster S, et al. An SPM8-based approach for attenuation correction combining segmentation and nonrigid template formation: application to simultaneous PET/MR brain imaging. *J Nucl Med.* 2014;55:1825-1830.

15. Burgos N, Cardoso M J, Thielemans K, et al. Attenuation correction synthesis for hybrid PET-MR scanners: application to brain studies. *IEEE Trans Med Imag.* 2014 33: 2332-41.
16. Dickson JC, O'Meara C, Barnes A. A comparison of CT-and MR-based attenuation correction in neurological PET. *Eur J Nucl Med Mol Imaging.* 2014;41:1176-1189.
17. Rousseau F, Habas PA, Studholme C. A supervised patch-based approach for human brain labeling. *IEEE Trans Med Imag.* 2011;30:1852-1862.
18. Buades A, Coll B, Morel JM. A review of image denoising algorithms, with a new one. *Multiscale Model Sim.* 2005;4:490-530.
19. Coupé P, Manjón JV, Fonov V, Pruessner J, Robles M, Collins DL. Patch-based segmentation using expert priors: Application to hippocampus and ventricle segmentation. *NeuroImage.* 2011;54:940-954.
20. Bai W, Shi W, O'Regan DP, et al. A probabilistic patch-based label fusion model for multi-atlas segmentation with registration refinement: application to cardiac MR images. *IEEE Trans Med Imag.* 2013;32:1302-1315.
21. Ye DH, Zikic D, Glocker B, Criminisi A, Konukoglu E. Modality propagation: coherent synthesis of subject-specific scans with data-driven regularization. *Lect Notes Comput Sc.* 2013;8149:606-613.
22. Kikinis R, Pieper SD, Vosburgh KG. 3D slicer: A platform for subject-specific image analysis, visualization, and clinical support. In: Jolesz FA, ed. *Intraoperative Imaging and Image-Guided Therapy.* New York, NY: Springer; 2014:277-289.

23. Torrado-Carvajal A, Hernandez-Tamames JA, Herraiz JL, Eryaman Y, Adalsteinsson E, Wald LL, Malpica N. Automatic segmentation pipeline for patient-specific MRI tissue models. *In Proc. Joint Annual Meeting ISMRM-ESMRMB*, Milano 10-16 may, 2014;22:4906.
24. Vunckx K, Dupont P, Goffin K, Van Paesschen W, Van Laere K, Nuyts J. Voxel-based comparison of state-of-the-art reconstruction algorithms for 18F-FDG PET brain imaging using simulated and clinical data. *NeuroImage*. 2014;102:875–884
25. Catana C, van der Kouwe A, Benner T, et al. Towards implementing an MR-based PET attenuation correction method for neurological studies on the MR-PET brain prototype. *J Nucl Med*. 2010;51:1431–1438.
26. Herraiz JL, España S, Cabido R, et al. GPU-Based fast iterative reconstruction of fully 3-D PET sinograms. *IEEE Trans Nucl Sci*. 2011;58:2257-63.
27. Delso G, Fürst S, Jakoby B, et al. Performance measurements of the Siemens mMR integrated whole-body PET/MR scanner. *J Nucl Med*. 2011;52:1914-1922.
28. Nakamoto Y, Osman M, Cohade C, et al. PET/CT: comparison of quantitative tracer uptake between germanium and CT transmission attenuation-corrected images. *J Nucl Med*. 2002;43:1137-1143.

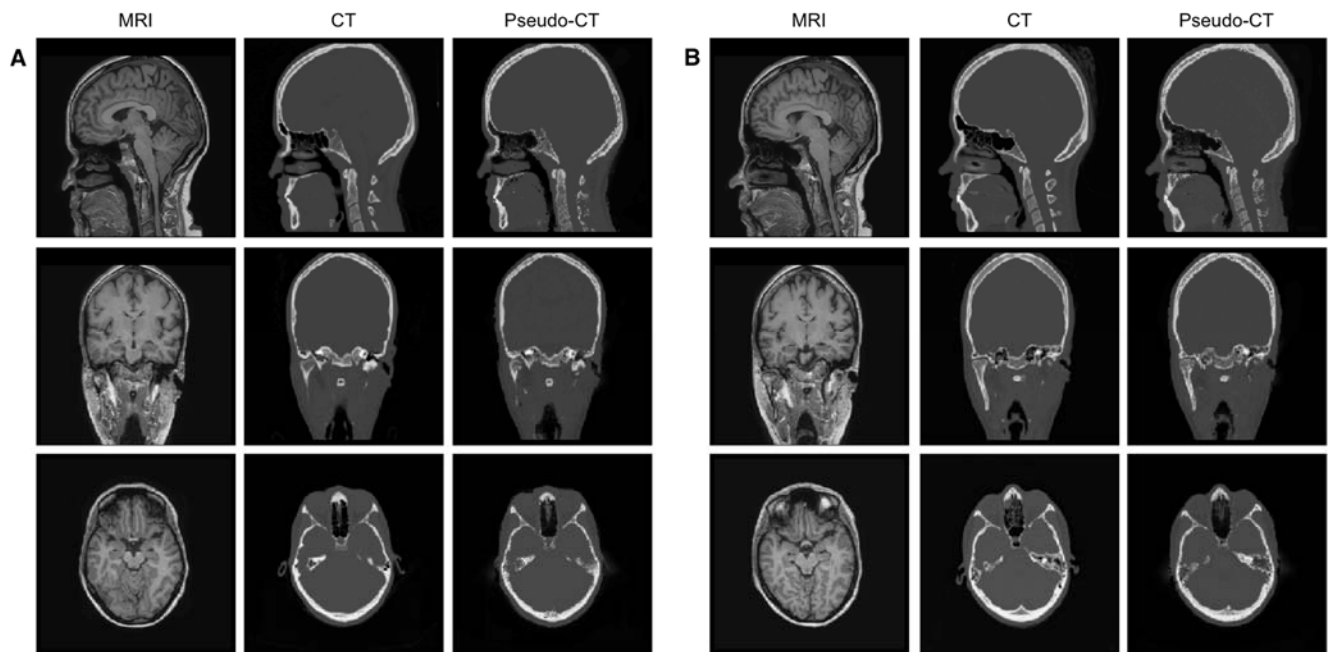


Figure 1. Sagittal, coronal and axial slices of the patient-specific MRI (first column), patient specific CT (second column), and synthesized pseudo-CT (third column) of two subjects.

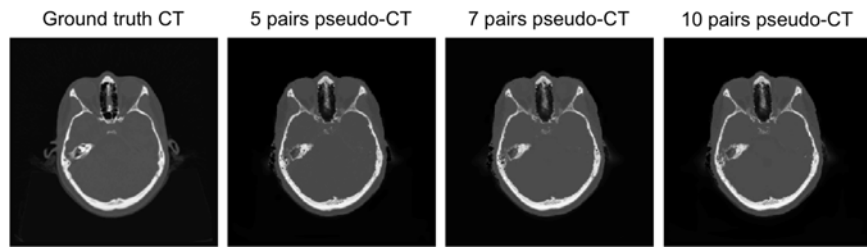


Figure 2. Axial slice of the patient specific CT and pseudo-CTs synthesized using atlases of different sizes.

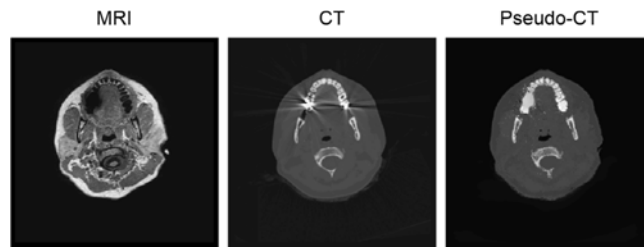


Figure 3. Artifacts caused by dental restorations. MRI (left) is impaired by signal loss; CT (centre) is impaired by beam hardening; pseudo-CT (right) is synthesized presenting some blurring in those zones.

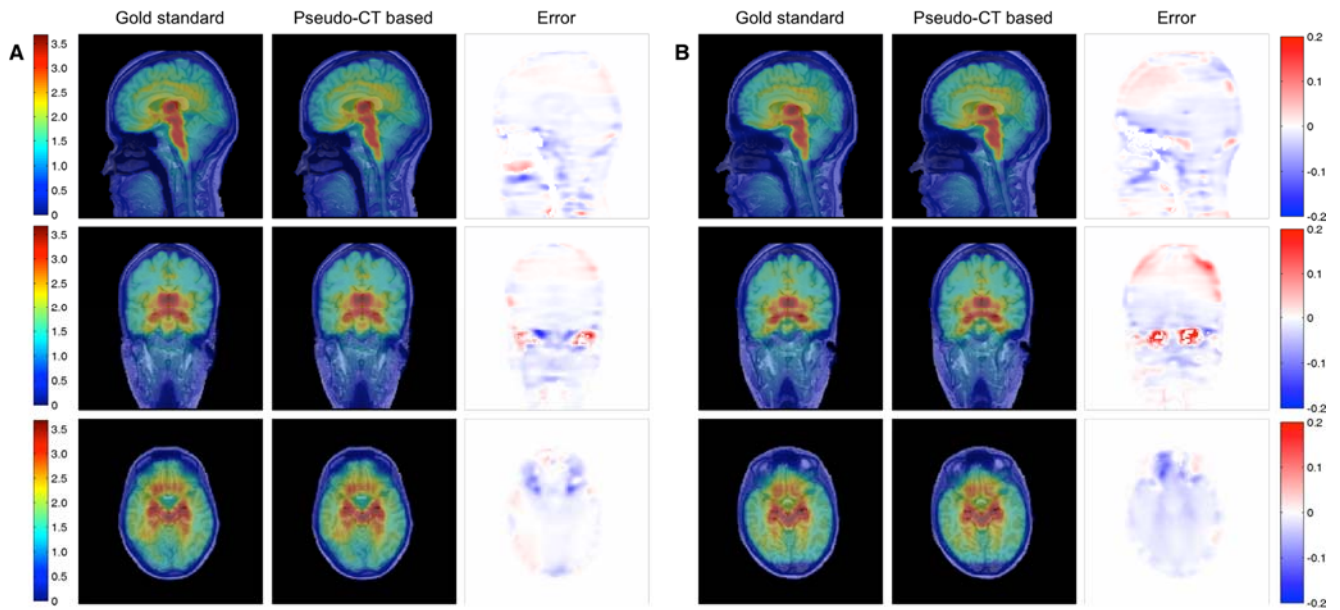


Figure 4. Sagittal, coronal and axial slices of the attenuation-free SUV volumes (first column), pCT-based corrected SUV images (second column), and error between both corrections (third column) for two subjects. Blue values in the error maps denote decreased PET SUVs in the pCT-based correction, while red values denote increased PET SUVs.

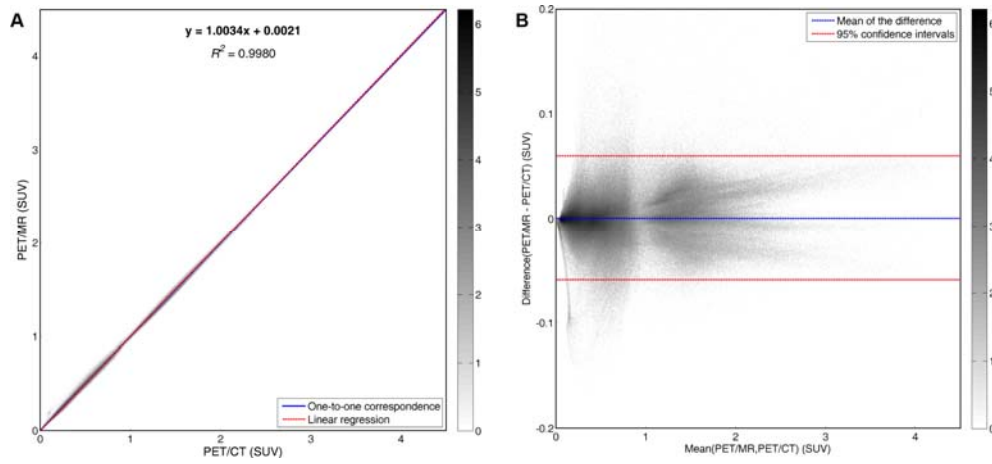


Figure 5. Voxel by voxel comparison of pCT-based attenuation correction against CT-based attenuation correction methods. The left plot shows the correlation between pCT-based SUV versus CT-based SUV from all subjects. The right plot shows the Bland-Altman of SUV measurements. Color bar shows density of voxels on histogram grid.

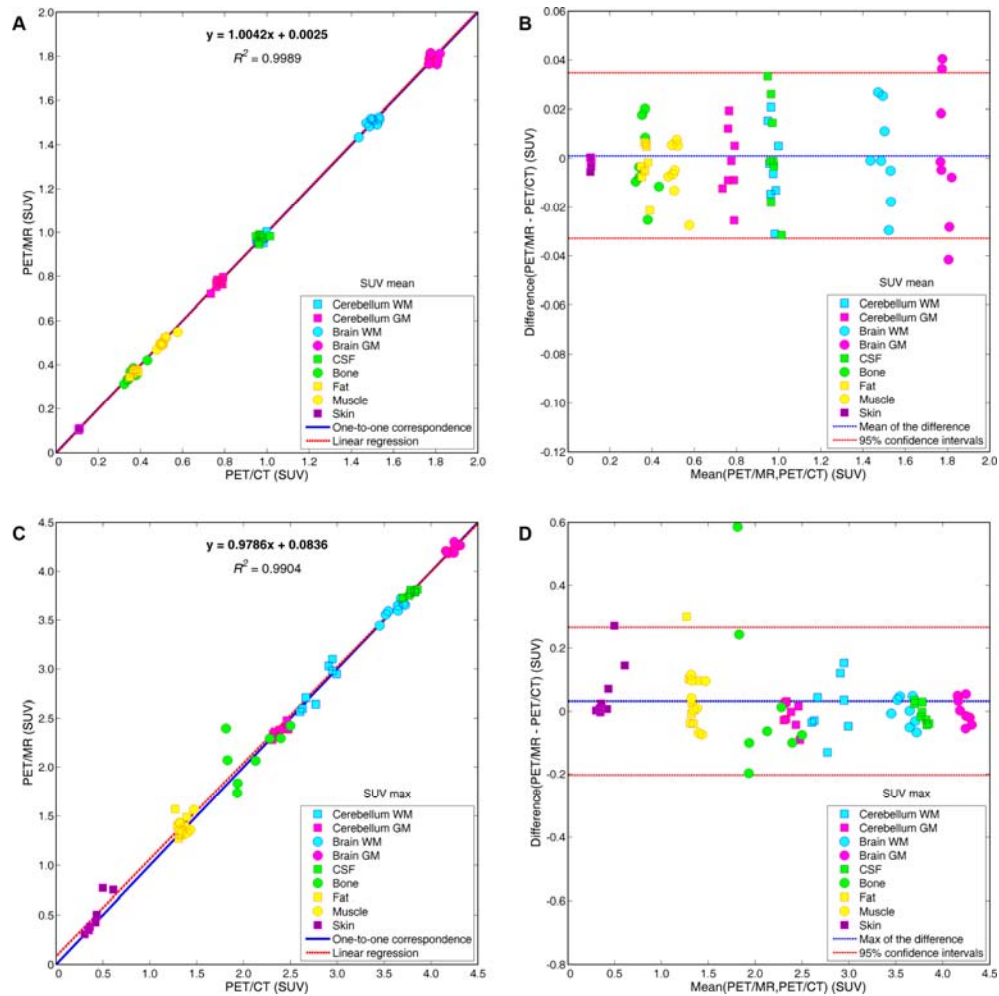


Figure 6. ROI comparison of pCT-based attenuation correction against CT-based attenuation correction. The left plots show the correlation between mean pCT-based SUV versus mean CT-based SUV (top) and max pCT SUV versus max CT-based SUV in the different tissues from all subjects. The right plots show the Bland-Altman of mean SUV and max SUV measurements.

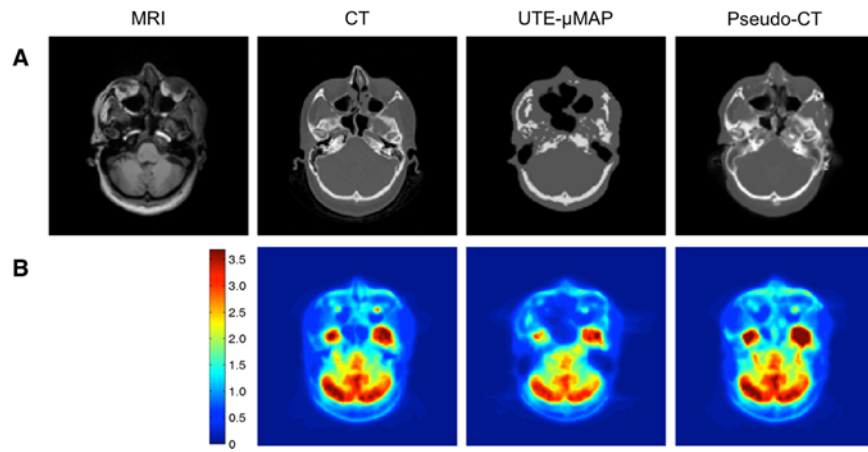


Figure 7. Axial slice of the MR, the CT, the UTE- μ MAP and the pseudo-CT volumes from clinical data (row A). Corrected SUV images using the different AC maps (row B).

ROI	pCT-based attenuation coefficient	CT-based attenuation coefficient	Absolute difference	p-value
Cerebellum WM	0.094554 ± 0.000324	0.094557 ± 0.000556	0.000004 ± 0.000570	0.7969
Cerebellum GM	0.094910 ± 0.002787	0.094919 ± 0.003018	0.000009 ± 0.002358	0.6289
Brain WM	0.094501 ± 0.000244	0.094468 ± 0.000512	0.000033 ± 0.000530	0.0938
Brain GM	0.094982 ± 0.004226	0.094942 ± 0.004577	0.000040 ± 0.003724	0.1211
CSF	0.094201 ± 0.006186	0.093993 ± 0.002647	0.000208 ± 0.005549	0.1406
Bone	0.171169 ± 0.039059	0.174073 ± 0.034212	0.002904 ± 0.028846	0.2383
Fat	0.096634 ± 0.013912	0.096558 ± 0.004161	0.000076 ± 0.012901	0.7969
Muscle	0.087851 ± 0.016329	0.087132 ± 0.004444	0.000719 ± 0.015747	0.1563
Skin	0.081767 ± 0.022670	0.087893 ± 0.009935	0.006126 ± 0.021313	0.0039

Table 1. Summary of mean pCT-based and CT-based attenuation coefficient values for each ROI analyzed. Within each ROI, mean pCT-based attenuation coefficient and standard deviation, mean CT-based attenuation coefficient and standard deviation, absolute difference and p-value obtained from the Wilcoxon signed rank test.

	Computational Time			
Volumes in Atlas	Matlab (days)	C (minutes)	C OpenMP (minutes)	GPU (minutes)
5	11.44	119.91 ± 0.02	61.76 ± 0.09	4.43 ± 0.00
7	16.18	168.08 ± 0.04	74.34 ± 0.29	6.20 ± 0.00
10	26.89	240.11 ± 0.14	99.84 ± 0.13	8.86 ± 0.00

Table 2. Comparison of the average ± standard deviation of the computational time spent to obtain a complete pCT volume using different implementations and atlas sizes. Matlab code was tested only once due to the computational cost.